



# Experimental Examination of Additively Manufactured Patterns on Structural Nuclear Materials for Digital Image Correlation Strain Measurements

K.A. Novich<sup>1,2</sup> · T.L. Phero<sup>1,2,3</sup> · S.E. Cole<sup>1,2</sup> · C.M. Greseth<sup>1,2</sup> · M.D. McMurtrey<sup>3</sup> · D. Estrada<sup>1,2,3</sup> · B.J. Jaques<sup>1,2</sup>

Received: 1 June 2023 / Accepted: 26 April 2024 / Published online: 20 May 2024  
© The Author(s) 2024

## Abstract

**Background** There are a limited number of commercially available sensors for monitoring the deformation of materials *in-situ* during harsh environment applications, such as those found in the nuclear and aerospace industries. Such sensing devices, including weldable strain gauges, extensometers, and linear variable differential transformers, can be destructive to material surfaces being investigated and typically require relatively large surface areas to attach (> 10 mm in length). Digital image correlation (DIC) is a viable, non-contact alternative to *in-situ* strain deformation. However, it often requires implementing artificial patterns using splattering techniques, which are difficult to reproduce.

**Objective** Additive manufacturing capabilities offer consistent patterns using programmable fabrication methods.

**Methods** In this work, a variety of small-scale periodic patterns with different geometries were printed directly on structural nuclear materials (i.e., stainless steel and aluminum tensile specimens) using an aerosol jet printer (AJP). Unlike other additive manufacturing techniques, AJP offers the advantage of materials selection. DIC was used to track and correlate strain to alternative measurement methods during cyclic loading, and tensile tests (up to 1100  $\mu\epsilon$ ) at room temperature.

**Results** The results confirmed AJP has better control of pattern parameters for small fields of view and facilitate the ability of DIC algorithms to adequately process patterns with periodicity. More specifically, the printed 100  $\mu\text{m}$  spaced dot and 150  $\mu\text{m}$  spaced line patterns provided accurate measurements with a maximum error of less than 2% and 4% on aluminum samples when compared to an extensometer and commercially available strain gauges.

**Conclusion** Our results highlight a new pattern fabrication technique that is form factor friendly for digital image correlation in nuclear applications.

**Keywords** Digital image correlation · DIC pattern fabrication · Tensile testing · Additive manufacturing

## Introduction

Real-time monitoring technology for structural materials is necessary to reduce the time to innovate in the nuclear and aerospace industries as defined by the United States Department of Energy's Nuclear Energy Enabling Technology

Program in 2011 [1]. More specifically, the current practice for materials in U.S. nuclear reactors is to examine structural components for in-pile deformation after being removed from operation, otherwise known as post-irradiation examination. In some cases, the materials must sit in pool storage or hot cells for an extended period of time prior to examination. The process is costly, time consuming and lacks the ability to observe the evolution of material degradation during a reactor power cycle [2]. There are only a few sensors that have been explored for measuring deformation in such harsh environments; including extensometers, strain gauges (SGs) [3–5], and linear variable differential transformers (LVDTs) [2]. While these devices offer good reliability and strain sensitivity, they also require direct contact with the substrate (a few require welding), which is destructive to the surface of the material and can alter its performance. Additionally,

✉ K.A. Novich  
kaeleenovich@u.boisestate.edu

✉ B.J. Jaques  
brianjaques@boisestate.edu

<sup>1</sup> Micron School of Materials Science and Engineering, Boise State University, Boise, ID, USA

<sup>2</sup> Center for Advanced Energy Studies, Idaho Falls, ID, USA

<sup>3</sup> Idaho National Laboratory, Idaho Falls, ID, USA

extensometers, SGs, and LVDTs have a large form factor and are limited to larger gauge lengths. For example, high temperature, axial extensometers are typically limited to gauge lengths of 10 mm or more for most manufacturers [6, 7].

Digital image correlation (DIC) is a non-contact, optical strain validation method that can solve such challenges. DIC uses image analysis to compare a reference image of a sample to images taken during a mechanical or thermal test using an iterative process with Gauss-Newton or Newton-Raphson algorithms. The technique is primarily used to track strain deformation, residual stress, and crack propagation [8–10]. Since it was first developed in the 1980s [11–13], DIC has grown in popularity in experimental mechanics because of its simplicity, cost effectiveness, and ease of implementation compared to other strain techniques [9, 14–18]. DIC has also been applied to various materials, including metals [19], ceramics [20], polymers [8, 21], and biological materials [22], from macroscopic to nanoscale [23–25]. In regard to the implementation of DIC in nuclear energy, there are some systematic challenges, including line of sight, lighting, irradiation, and image resolution. For most engineering applications, 2D DIC is used, where the camera lens is placed perpendicular to the surface being investigated. Any misalignment or out-of-plane displacements of the camera will cause error in measurement readings [26–28]. The surface must be visible to the camera to track changes in elongation, and as such, some DIC setups require external lighting [18, 29]. Materials inside a nuclear reactor are likely to experience degradation from irradiation effects and the materials used in the DIC patterns would need to sustain such conditions. Lastly, DIC depends on image quality, which improves with advancements in camera technology [30].

There are three main components to the implementation of 2D DIC: pattern fabrication, DIC test setup (e.g., 2D DIC or 3D DIC), and displacement and strain field computation [9, 14]. The following work focuses on the optimization of pattern fabrication.

Literature suggests that a good quality DIC pattern is one that has high contrast, randomness, isotropy (i.e., speckles and space between speckles are the same size in all directions), and strong adherence to the testing surface [9, 10, 14, 31–33]. Random-based patterns are commonly fabricated using aerosol spray painting techniques due to ease of application and cost effectiveness [14]. Speckle size distribution depends on nozzle diameter, nozzle shape, the distance of the nozzle from the substrate, pressure, and viscosity of solution. However, there are limitations to splattering techniques; such as inconsistencies in size and distribution in speckles, difficulty of reproduction, and dependence on the operator.

Other methods that have been used to create DIC patterns include spin coating [34], compressed air [35], nano-film remodeling [36], lithography [37], focused ion beam [38],

scratching and abrading [39], and laser engraving [40]. Of the following options, laser engraving produced patterns offer controllable size, density, depth, and distribution of speckles [32, 41]. While achieving good consistency, laser engraving is limited to certain applications where the material itself provides a high contrast pattern. Accordingly, a good pattern is one that identifies changes in displacement without cracking, detaching, or affecting the mechanical properties of the test specimen. All the patterns listed above have one or more restrictions to producing a pattern that meets all the requirements, which has made it difficult to commercialize DIC.

Additive manufacturing (AM) capabilities are a viable solution to high quality DIC patterns for planar, curved, and flexible substrates [4, 42]. Printing techniques allow the user to control the entire fabrication process of the DIC pattern. Additionally, AM provides easily repeatable patterns and allows for a wider material selection that can be selected based on the application. In 2022, Zhu et al. used a handheld inkjet printer to develop a random, fluorescent speckle pattern that resulted in better image analysis compared to spraying methods [43]. The authors found speckle sizes ranged from 90 to 150  $\mu\text{m}$  in a 32 mm  $\times$  40 mm field of view with a 5-megapixel camera. In 2019, Koumlis et al. [44] also used inkjet printing for DIC pattern fabrication to create periodic and pseudo-random patterns on tensile specimens. The DIC results calculated from the images of these patterns taken during mechanical tests were then compared to the strain correlating to spray-painted random patterns [44]. The strain calculated from Koumlis's printed patterns had minimal error to strain measured by an LVDT during experiments. Besides inkjet printing, Yang et al. in 2021 proposed 3D printing using a fused deposition modeling type of printer to create random patterns [45]. Their printed speckles were between 100 and 200  $\mu\text{m}$ , which limits the fabrication technique to macro-scale DIC applications. Unlike previous AM work for DIC systems, we demonstrate the use of aerosol jet printing (AJP) to develop a wider selection of DIC patterns, which has the ability to print materials with viscosities ranging from 1 to 1000 cP. Comparatively, inkjet is limited to viscosities below 20 cP [46]. The increase in ink flexibility makes aerosol jet printed patterns more appealing to harsh environment applications, such as nuclear reactors, than patterns developed using inkjet printing techniques.

Furthermore, our study investigated the computational feasibility of DIC patterns with periodicity. Periodic patterns are easy to program and implement in printing techniques [44] comparatively to spray-painted patterns. Additionally, patterns that contain periodicity have lower gray level distributions between the reference image and images taken during tests, otherwise known as noise propagation or optical residual, and theoretically should equate to less error in strain and displacement fields created by DIC algorithms

[47]. However, literature typically recommends random based patterns to obtain optimal full-field displacement mapping [9, 14, 16, 28, 31, 32] because the absolute minimum of the optical residual associated with periodic patterns is difficult to find, and as such, an initial guess that is typically needed to commence the iterative process is not feasible [47]. While historically this is correct, recent literature, as shown in [44], indicates that DIC adequately computes periodic patterns. Firstly, DIC can process periodic patterns when the actual displacement measured is not greater than the period of the repetitive pattern sequence [48]. Second, adding defects to periodic patterns or creating pseudo periodic patterns resolve any convergences at the local minimum during computation. Lastly, modifications to DIC algorithms make it possible to process images of DIC patterns with lower levels of randomness. The work presented below adds to the validity of patterns containing levels of periodicity being used in DIC systems through comparing such patterns to random spray-painted patterns.

Now, tracking displacements with periodic patterns is not a new concept. Early periodic patterns composed of intersection of lines or dots was documented in the 1940's–1960's, where changes in pattern were measured by hand [49]. Today, tracking displacements is performed computationally and periodic patterns are primarily used in the grid method (GM) and Moiré Interferometry, where lines are used to form fringe patterns [50]. GM relies on a windowed Fourier transform through localized spectrum analysis to extract phase distributions from patterns, which are then correlated to changes in displacement [51]. There have been multiple comparison studies between DIC and the grid method in

recent years and these studies conclude that the grid method was useful for small strain analysis, while DIC was best for all other cases [51–53]. In addition, a majority of these comparison studies, as described above, were performed with simulations rather than with physical experiments. The objective of this study is not a comparison between the two methods, but rather fabricating similar patterns used in the grid method and applying them to DIC in tensile loading experiments to examine its computational feasibility.

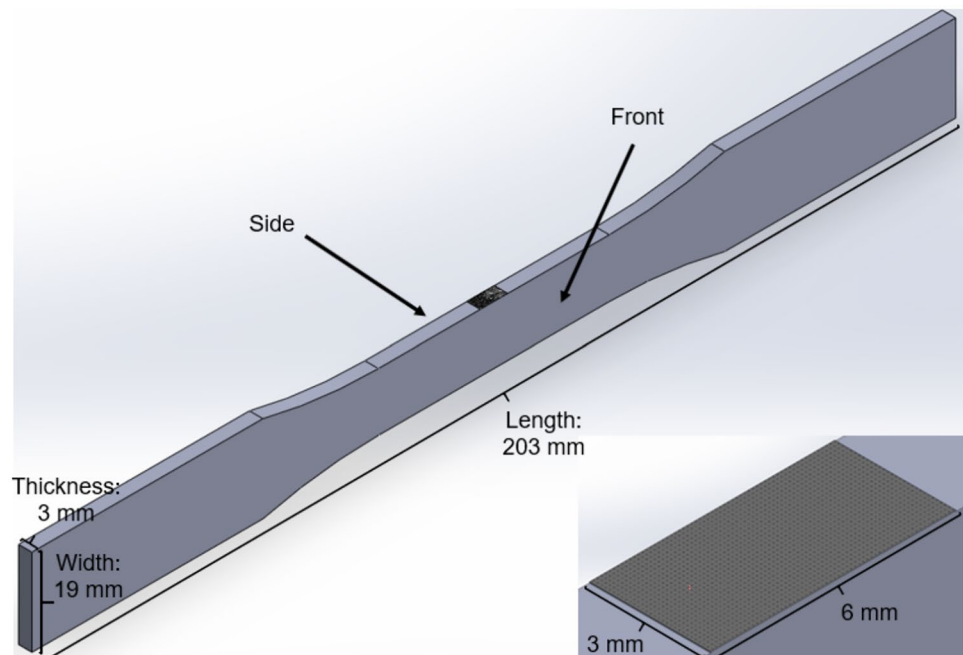
## Method

The desired DIC patterns were fabricated using an aerosol jet printer and were printed directly on the sample surface as described in more detail in “[Materials and DIC Pattern Fabrication](#)” section. Mean intensity gradient and grayscale intensity analysis was used to optimize the computational feasibility of the patterns before testing. Tensile specimens with the printed patterns were mechanically tested following a 2D DIC setup.

## Materials and DIC Pattern Fabrication

Periodic patterns were fabricated by first applying a black background on the sides of ASTM E8/E8M – 16a standard [54] compliant stainless steel (SS316L) and aluminum (Al6061) test specimens with commercially available spray paint (high temperature silica ceramic coating, Helix Racing Products, temperature rating: 704–1093 °C) as shown in Fig. 1. SS316L and Al6061 are typically used as nuclear

**Fig. 1** Schematic of tensile test specimens with printed DIC pattern. DIC patterns were printed on the sides of samples and were 6 mm × 3 mm in size



materials due their mechanical properties and high corrosion and irradiation resistance [55–57]. Prior to this step, the sides of the as-received tensile test specimens were ridged and non-planar due to electrical discharge machining. As such, samples were ground down with 180 grit silicon carbide paper to provide a smooth, homogeneous surface. A smooth surface was necessary to achieve consistent periodicity of the pattern when printing. SS316L and Al6061 were chose to check the ability of the DIC algorithm to process periodic patterns on two materials with different mechanical properties. Line and dot patterns were printed onto the sides of the test specimen (i.e., one type of pattern on each side) using an AJP (Aerosol Jet Series 200, Optomec) with silver nanoparticle ink (PRELECT-TPS 50G2, Clariant). Silver ink was chosen for the printed patterns due to its bright white appearance after being cured.

The ink was diluted with DI water at a 1:3 volumetric ratio in a glass vial for ultrasonic atomization as recommended by studies using AJP to create electronic material before printing [5, 58–60]. Approximately 1.2 mL of ink was used during each print session to fabricate 4 patterns with dots and 4 patterns with lines. An additional 18.5 mL of DI water was added to the solvent bubbler, which is an extra vile on the AJP that is integrated in the aerosol gas line to help prevent solvent evaporation that may occur while printing [61] Table 1 highlights the parameters that were used to print patterns.

A total of 8 test specimens (i.e., four Al6061 and four SS316L) were printed on with the four independent pitch sizes in a 3 mm × 6 mm field of view. Pitch sizes were selected as 250 μm, 150 μm, 100 μm, and 50 μm to investigate the effects of contrast between black and white pixels on DIC image processing. ImageJ was used to quantify each printed pattern [62], as described in the next section. The average sizes of the dot and line printed patterns are shown in Table 2. The optimization of the print parameters varied with time during single prints due to clogging in the nozzle system. After printing, each pattern was cured at 200 °C for 1 h on a hot plate in a fume hood at ambient conditions. Moreover, a randomized speckle pattern was spray-painted on Al6061 and SS316L substrates to compare to the printed patterns. Each type of DIC pattern is shown in Fig. 2.

**Table 1** AJP printing parameters for pattern fabrication

AJP Printing Parameter	Value (Units)
Deposition Head Nozzle Size	100 μm
Sheath Gas (N <sub>2</sub> ) Flow	15 sccm
Ultrasonic Atomizer Gas (N <sub>2</sub> ) Flow	21–22 sccm
Ultrasonic Atomizer Current	500 mA
Printing Speed	4 mm/s
Platen Temperature	20 °C
Water Bath Temperature	22 °C

**Table 2** Printed dot diameters and line thicknesses for different pitches

Printed Pattern Type	Pitch Sizes (μm)	Dot Diameter/ Line Thickness (horizontal/vertical), (μm)
Dots	50	30 ± 9
	100	48 ± 11
	150	41 ± 7
	250	34 ± 5
Lines	50	32 ± 4/32 ± 4
	100	32 ± 4/33 ± 5
	150	37 ± 5/33 ± 5
	250	31 ± 3/30 ± 1

In addition to the printed patterns, commercially available resistive SGs (HFH-12-250-ZHW, Hitec Products, 120 Ω wire) were bonded to each tensile test specimen using a ceramic cement (NCC-3 and HG-1, Hitec Products). Refer to Phero et al. regarding strain gauge bonding process [5].

## DIC Pattern Analysis

To confirm the DIC patterns were of good quality, two pattern assessment techniques were performed: mean intensity gradient (MIG) and grayscale intensity analysis. The MIG is a global parameter that evaluates the entire pattern and estimates the precision between measured and actual displacements [14]. There are two primary measurement errors associated with DIC calculations: random and systematic errors [50]. The random error is related to the standard deviation of the measured displacement, while the systematic, or mean bias, error is the difference between actual imposed displacement on a specimen and the mean measured displacement. Periodic patterns have lower random and systematic errors compared to random patterns because periodic patterns typically have gray level distribution gradients that are maximized [47, 48]. Pan et al. developed MIG in 2010 and found a higher MIG correlated to a lower mean bias error and standard deviation error [16, 31, 32, 34]. The mean intensity gradient is defined as

$$MIG = \sum_{i=1}^W \sum_{j=1}^H \left| \nabla f(x_{ij}) \right| / (W \times H) \quad (1)$$

where  $W$  is the image width in pixels,  $H$  is the image height in pixels, and  $\left| \nabla f(x_{ij}) \right|$  is the local intensity gradient vector, which is found by taking the magnitude of the x- and y-directional intensity derivatives. The directional intensity derivatives are found using a gradient operator (i.e., a prewitt operator or a central difference algorithm) [16].

Grayscale analysis was used to assess the black and white pixel intensity contrast of the pattern [10, 16, 34]. Images



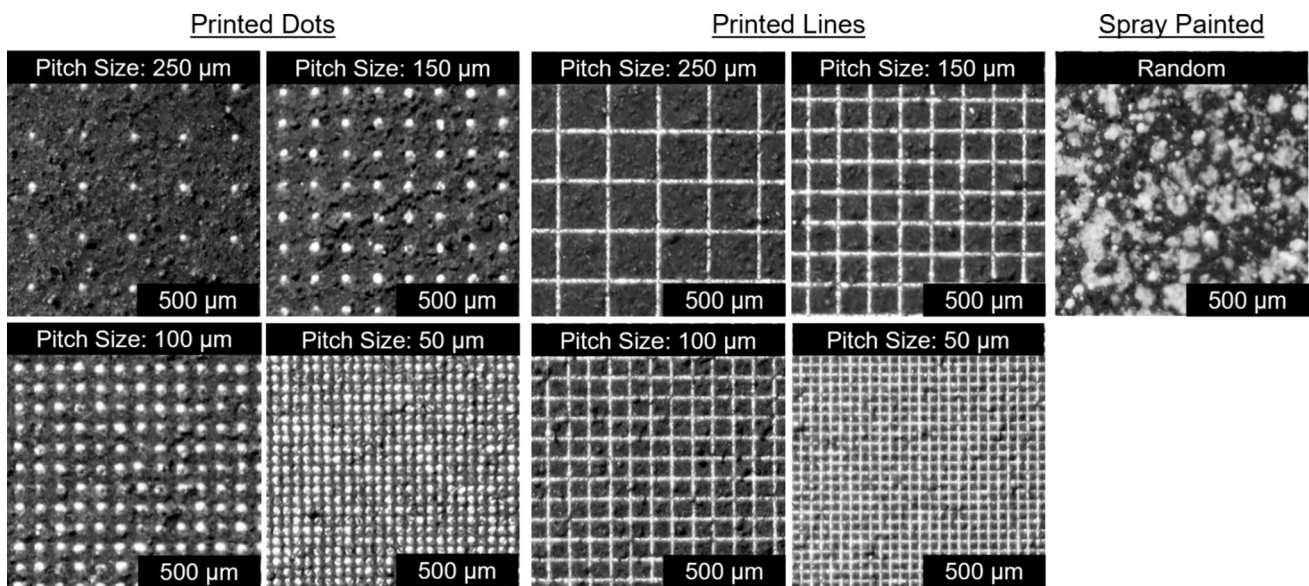


**Fig. 2** Dot and line printed patterns with 250  $\mu\text{m}$ , 150  $\mu\text{m}$ , 100  $\mu\text{m}$ , and 50  $\mu\text{m}$  pitch sizes. The printed patterns were also compared with a randomized spray-painted pattern, similar to the image shown on the right

of the patterns at the region of interest had a resolution of  $1548 \times 810$  pixels and were converted to 8-bit using ImageJ. For an 8-bit image, the gray level intensity ranges from 0 to 255, which correlates to black and white colors. The data was then extracted and the number of pixels were plotted against the gray-level intensity. A pattern with high contrast will have two prominent peaks near 0 and 255 pixel intensities. The contrast of patterns and brightness of images will affect MIG values and grayscale analysis and must be selected carefully [16].

### Mechanical Test Setup

Tensile experiments were performed using a mechanical test fixture (MTS Series 793) that was equipped with an axial extensometer (MTS Model 632.53E-11), which was calibrated using the ASTM E83 Class B1 standard. Test specimens were subjected to cyclic tensile loads at a strain rate of 9–10  $\mu\text{E}/\text{sec}$  for SS316L specimens and 13–14  $\mu\text{E}/\text{sec}$  for Al6061 specimens, following similar guidelines found in ASTM E251 92 [63] and ASTM E83 16 [64] as suggested by ASTM E2208-02 standard [65]. Commercially available resistive SGs were bonded to each test specimen and was measured using a three-wire quarter-bridge configuration. The setup was carried out on a NI-PXI 1071 controller with a NI-PXIe-4330 Strain Bridge Module similar to the experimental setup found in Phero et al. [5].

Images were taken using a digital single-lens reflex camera (Canon EOS 90D) with a 60 mm macro lens to increase the magnification and detail of the small field of view (3 mm  $\times$  6 mm). The camera was placed perpendicular to the test

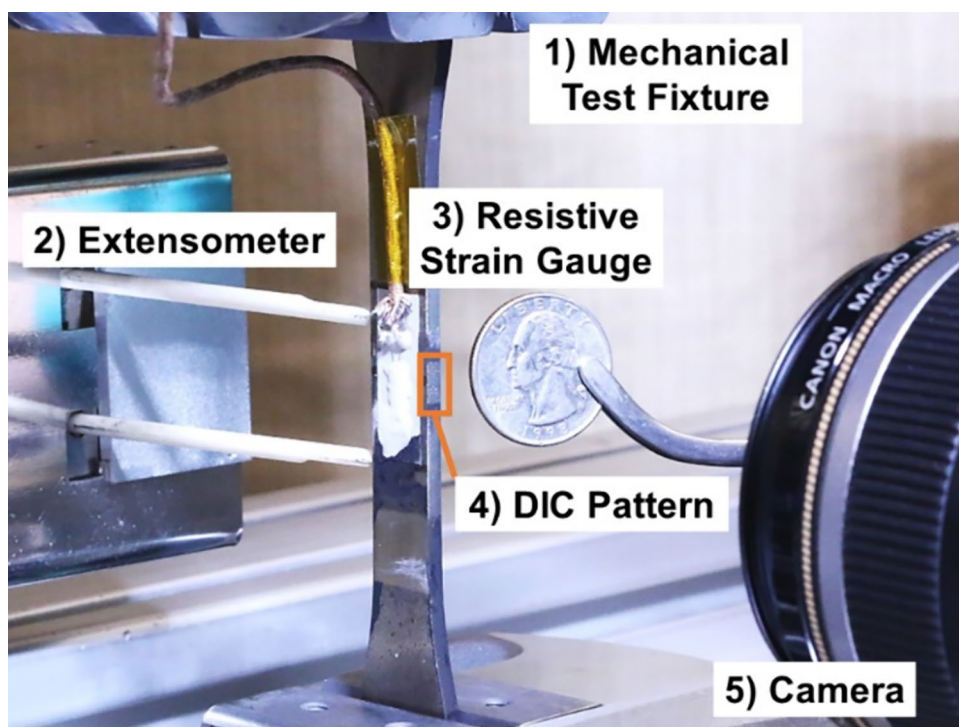
specimen following a 2D DIC setup, while the extensometer was firmly placed directly on the other side of the DIC printed pattern as shown in Fig. 3. Reference images were taken after the tensile test specimens were loaded into the mechanical test fixture and the camera lens was manually focused onto the pattern. During experiments, images were taken every 20 s for SS316L samples and 15 s for Al6061 samples since the materials had to be pulled at different loads to achieve the desired strain. The images were captured remotely to avoid causing external vibrations to the camera. The camera settings used during experiments are shown in Table 3. A 24W LED floodlight was placed to the left side of the camera and was configured to provide white light at 2000 lumens.

### Image Analysis

Images were analyzed using the Ncorr platform (version 1.2), an open source DIC software, on Matlab R2019b. Ncorr uses an inverse compositional Gauss-Newton (IC-GN) algorithm to identify displacement fields and relies on a C++ compiler [66]. The IC-GN algorithm is similar to the forward additive Newton-Raphson algorithm, which reduced the redundancy in traditional DIC computational methods. However, the IC-GN is more efficient at determining full-field displacements due to the use of a Hessian matrix that is pre-computed and remains constant through the computation [67].

Once the reference image and the images taken during testing are uploaded to the software, a rectangular region

**Fig. 3** The digital image correlation setup used during experiments. The tensile test specimen was loaded into the mechanical test fixture with the DIC printed pattern side facing the camera, which was located 60 mm away. The extensometer was placed on the opposite side of the tensile specimen in the same gauge length region. A strain gauge was bonded to the front face of the test specimen. A quarter was brought to the printed pattern to highlight the small field of view (6 mm × 3 mm)



of interest was chosen around the pattern and the subset location was placed in the middle of the region. The subset radius was selected as 44 pixels with a spacing of 3 pixels in Ncorr. Seeds were then placed near the four corners of the region of interest. The algorithm typically takes between 10 and 19 iterations to identify displacement measurements. For calibration and scaling, the known thickness (3 mm) of the side of the test specimen was inputted into the software and a strain radius of 12 pixels was selected based on suggestions described in Ncorr's manual and in literature [66, 68, 69]. The strain average was then recorded from the contour plots established for each image. The same subset radius, subset spacing, and strain radius was used for both printed and spray-painted patterns.

The strain values computed by Ncorr are Green-Lagrangian strains [66]. There is also an option in Ncorr to observe strain values in Euler-Almansi. Green-Lagrangian and Euler-Almansi strains are typically used in finite-element applications to track displacements. Green-Lagrangian strains correlate to the material coordinates of the body being

investigated and Euler-Almansi uses spatial coordinates. Refer to *Finite Element Applications: A Practical Guide to the FEM Process* by Okereke and Keates regarding different strain tensors used to find displacement fields [70]. At relatively small displacements, all strain types will have the same strain measurement, and as such, the Green-Lagrangian strains from Ncorr were directly compared to the engineering strain values recorded by the extensometer.

## Results

The results focus on the mean intensity gradient and grayscale analysis of the printed patterns as well as pattern performance at measuring strain. Based on the DIC pattern analysis, all printed patterns were recognizable by the DIC algorithm. Printed patterns were compared to spray-painted patterns and validated using an extensometer and strain gauges.

### Mean Intensity Gradient and Grayscale Intensity Analysis of Printed Patterns

The DIC pattern analysis, such as MIG and grayscale intensity, was used to predict the computational feasibility of the printed patterns. The calculated MIG values for printed and spray-painted patterns using equation (1) is found in Table 4. All patterns had a mean intensity gradient above 20, which would indicate the patterns should have a low mean bias

**Table 3** Camera setting parameters for DIC experiments

Property	Value (Units)
Resolution Width	6960 pixels
Resolution Height	4640 pixels
Aperture Size	f/2.8
Exposure Time	1/125 sec
ISO	2500

**Table 4** MIG values for the printed and spray-painted DIC patterns on SS316L substrates

Printed Pattern Type	Pitch Sizes ( $\mu\text{m}$ )	Mean Intensity Gradient
Dots	50	87
	100	47
	150	46
	250	24
Lines	50	98
	100	75
	150	71
	250	51
<b>Spray-Painted Pattern</b>		42

error and low standard deviation error [16]. The lowest MIG values for both line and dot printed patterns were observed for the 250  $\mu\text{m}$  pitched patterns. The MIG increased as more lines and dots were added to the printed region, with the 50  $\mu\text{m}$  pitch patterns having the highest values. The random spray-painted speckle pattern had a lower MIG value compared to the printed patterns (with the exception of the 250  $\mu\text{m}$  pitch dot pattern, which was 57% lower).

Figure 4 shows the grayscale intensities of the printed and spray-painted DIC patterns. All patterns exhibit a prominent peak towards the black spectrum of pixel intensity because the pattern background (the substrate) was black. Based on previous studies [14, 27, 71], there is no difference in strain measurement quality between black-on-white or white-on-black patterns. The printed patterns gained more pixels in the white intensity spectrum with decreases in pitch size that allowed for more dots and lines in the region of interest. The 50  $\mu\text{m}$  pitch patterns had the least noticeable peaks and pixels were found to be gray rather than having a high contrast between black and white pixels. The random spray-painted, the 150  $\mu\text{m}$  pitch lines, and the 100  $\mu\text{m}$  pitch dots were the only patterns to have two peaks and were assumed to be the best quality patterns.

### Printed Pattern Performance

Tensile tests were performed on SS316L and Al6061 samples to investigate the accuracy of DIC strain measurements to other strain sensors and the precision of the DIC strain results (measured displacement) to follow the cyclic tensile profile observed by the extensometer (actual displacement). Nine tests were performed with each printed DIC pattern (i.e., six tests with SS316L and three tests with Al6061). As seen in Fig. 5, all the DIC patterns on the SS316L substrates displayed higher strains when correlated to the elongation found by both the extensometer and strain gauges. More specifically, the larger strain difference was observed

at the top of each cycle. Both the relative error at the largest strain difference and statistical significance ( $p$ -value) was found from the strain calculated by the DIC and compared to the measurements of the extensometer and strain gauges (Table 5). Based on the statistical analysis, there is no significant difference between the DIC results and the data from the extensometer since all  $p$ -values were found to be greater than 0.05. As such, the 150  $\mu\text{m}$  spaced lines and 100  $\mu\text{m}$  spaced dots produced accurate strain values to the extensometer and strain gauges.

The same experiments were performed on Al6061 tensile test specimens. Strain values computed from most DIC patterns were above the readings from the other strain measurement methods, except for the 100  $\mu\text{m}$  and 50  $\mu\text{m}$  pitched lines (Fig. 6). Table 5 highlights the error and statistical significance from the results. The 150  $\mu\text{m}$  pitched lines and the 100  $\mu\text{m}$  pitched dots correlated to strain values that had a relative 4% and 2% difference to the data from the other strain measurements. Similar to the results from the SS316L samples, a statistical analysis was performed between the DIC data and the extensometer. The  $p$ -values correlating to all DIC patterns was greater than 0.05, and as such, there was no significant difference between the strain measurements used in this study.

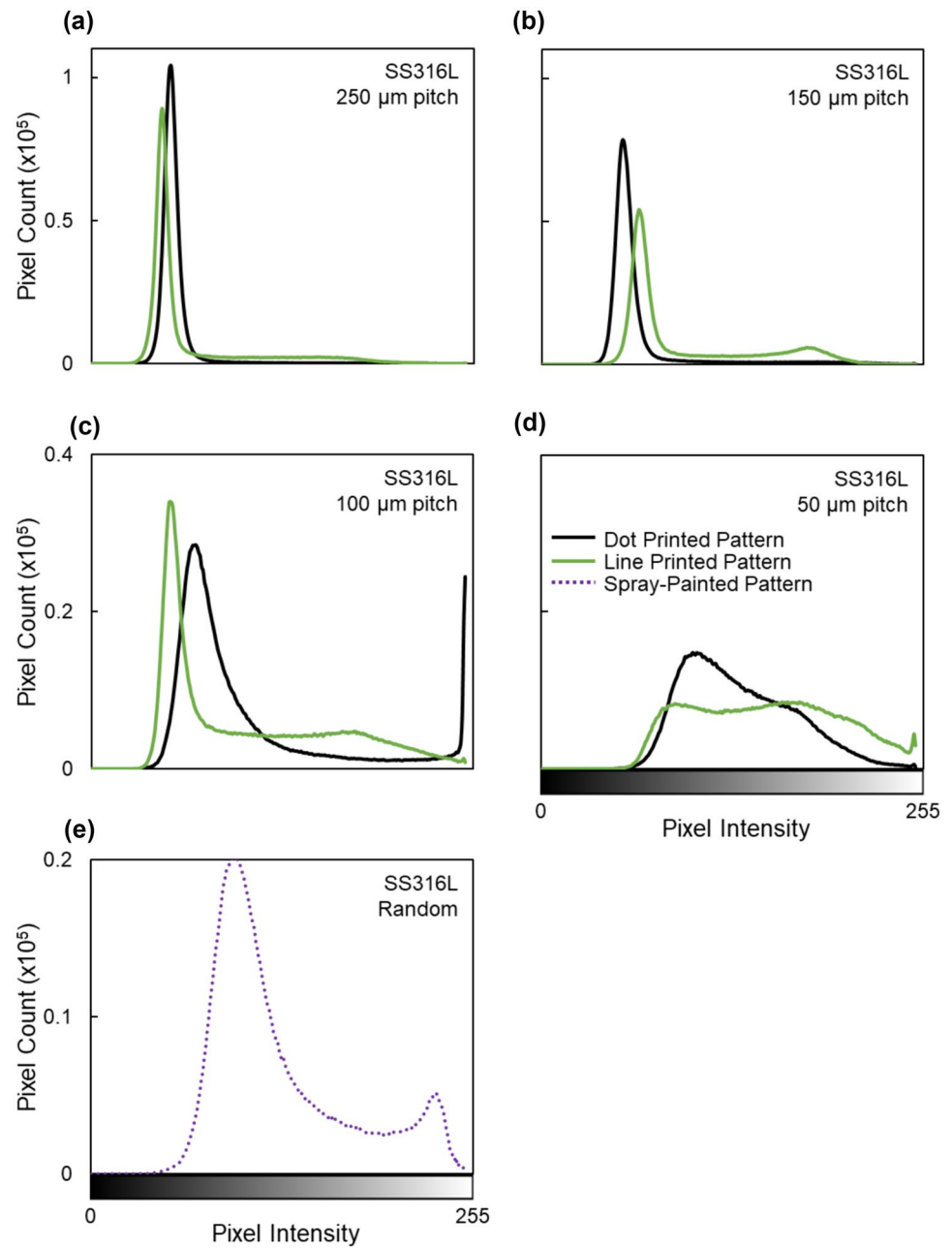
Additionally, spray-painted patterns were placed on SS316L and Al6061. Four tests were performed on each material. The DIC strain measurements calculated from the spray-painted patterns correlated to the extensometer and the strain gauges. More specifically, the strain correlated to the spray-painted samples on aluminum tensile specimens had a 4% difference and  $p$ -value of 0.87 from the strain measured by the extensometer and strain gauges (Table 5) (Fig. 7).

In order to better understand the use of DIC for finding mechanical properties of materials, the Young's modulus was found by dividing the force (recorded by the mechanical test frame) by the cross-sectional area of the tensile test specimen and applying Hooke's Law. Hooke's Law was defined as

$$\sigma = E\epsilon \quad (2)$$

where  $\sigma$  was the stress,  $E$  is the Young's modulus, and  $\epsilon$  is the strain. Accordingly, each sample was only strained within the elastic region of the stress-strain curve throughout the entire test. For the SS316L test specimens, the printed and spray-painted patterns correlated to strain values that displayed a lower Young's modulus than what is found in literature when using equation (2), as shown in Fig. 8(a) [72–74]. However, the elastic modulus calculated using the DIC strain values from most of the patterns were near 170 GPa. Only the DIC strain from the pattern with the 150  $\mu\text{m}$  line pitch resulted in an average modulus of elasticity of 203 GPa, which was in the desired region for

**Fig. 4** Grayscale analysis for the printed (a) 250  $\mu\text{m}$  pitch, (b) 150  $\mu\text{m}$  pitch, (c) 100  $\mu\text{m}$  pitch, and (d) 50  $\mu\text{m}$  pitch patterns and for the (e) spray-painted pattern. Images of each DIC pattern had a pixel count of  $1.2 \times 10^6$  pixels. The printed 150  $\mu\text{m}$  pitch line pattern, the printed 100  $\mu\text{m}$  pitch dot pattern, and the spray-painted pattern had two peaks



SS316L and matched well with the moduli found using the strain measurements from the extensometer and strain gauges (Fig. 8(a)). Similar results were observed using the strain calculated from the DIC patterns on Al6061 substrates where overestimation of strain calculated by the DIC algorithm led to smaller Young's modulus values (Fig. 8(b)). All strain values computed from the patterns corresponded to below the expected Young's modulus value of 69.9 GPa for Al6061-T6 [72]. A majority of the results from the strain measurement techniques were found

to have a Young's Modulus be between 60 and 70 GPa when using equation (2).

The coefficient of determination ( $R^2$ ) was determined based on the strain measurements from each pattern on SS316L and Al6061 across all tests performed. The results from the patterns were plotted against the data from the extensometer and the average was taken to get the coefficient of determination. Accordingly, the strain values computed from the DIC patterns had a  $R^2$  of 0.97 or higher, which would indicate good accuracy (Table 6).



**Fig. 5** The comparison of strain as measured by DIC, strain gauges, and an extensometer on SS316L, as well as dot and line pattern with varied spacing, including (a) 250  $\mu\text{m}$  pitch, (b) 150  $\mu\text{m}$  pitch, (c) 100  $\mu\text{m}$  pitch, and (d) 50  $\mu\text{m}$  pitch. Error bars were found by calculating the standard deviation from the six tests performed with each pattern type

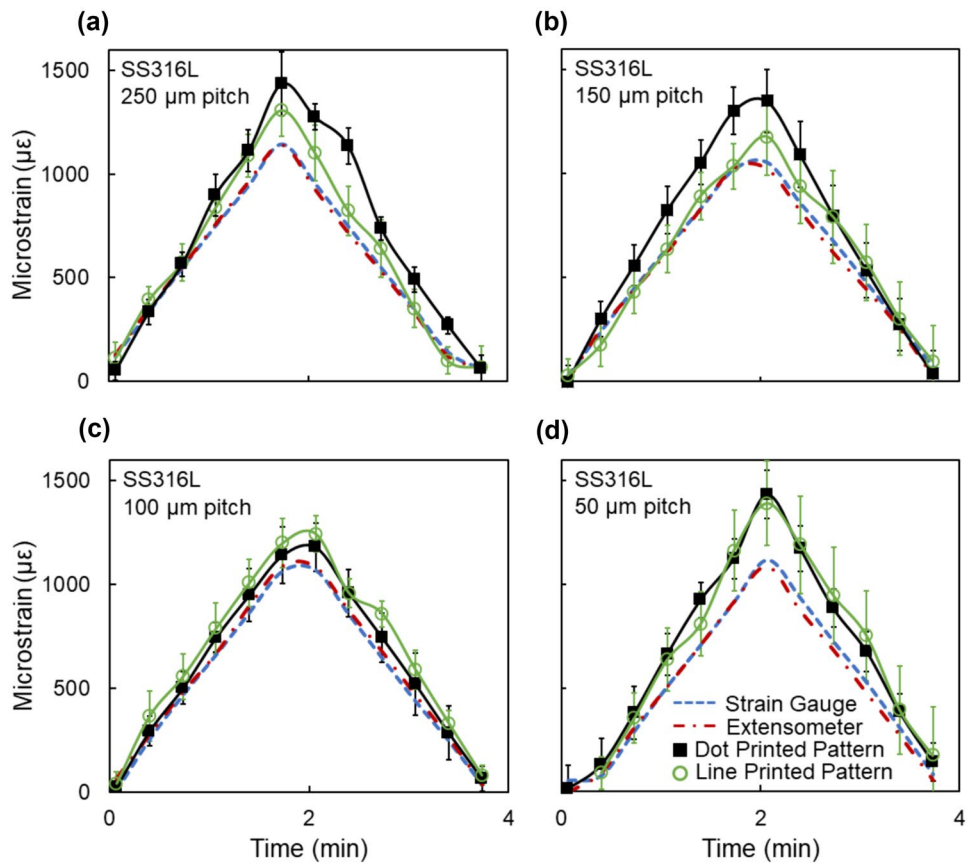


**Fig. 6** The comparison of strain as measured by DIC, strain gauges, and an extensometer on Al6061, as well as dot and line pattern with varied spacing, including (a) 250  $\mu\text{m}$  pitch, (b) 150  $\mu\text{m}$  pitch, (c) 100  $\mu\text{m}$  pitch, and (d) 50  $\mu\text{m}$  pitch. Error bars were found by calculating the standard deviation from the three tests performed with each pattern type

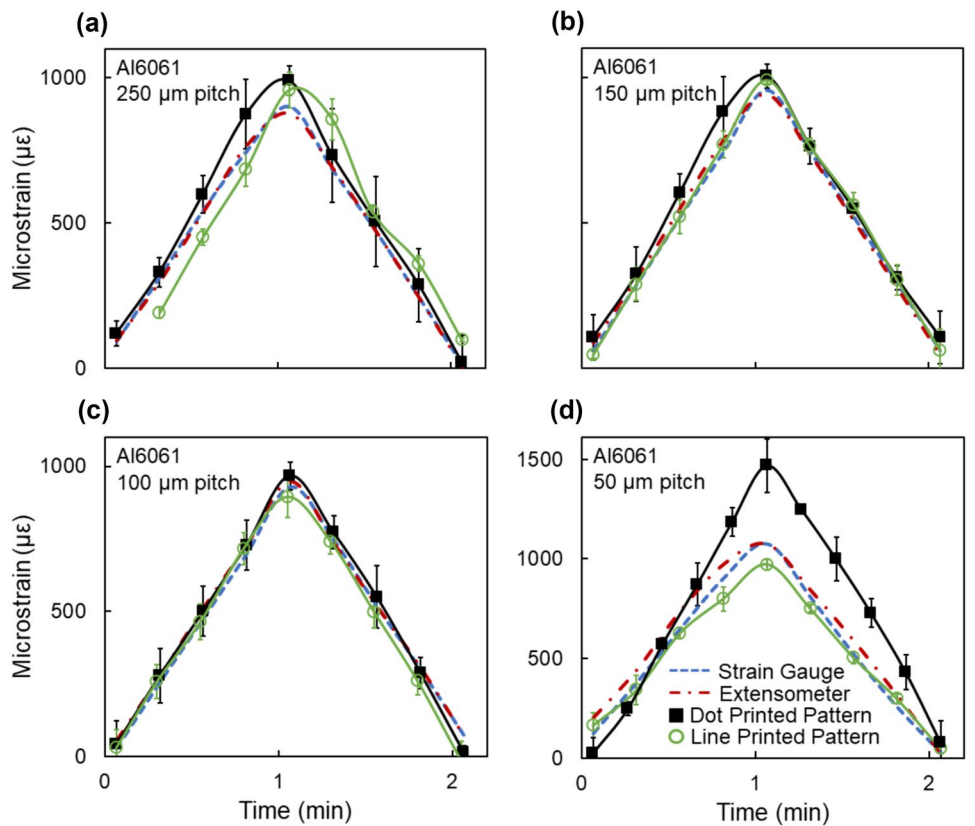
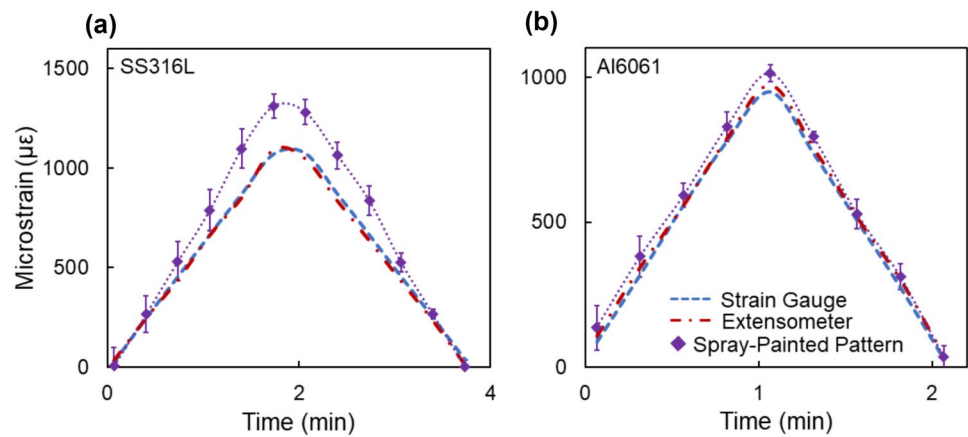


**Fig. 7** The comparison of strain estimated by DIC from the spray-painted patterns to the extensometer and strain gauges on (a) SS316L and (b) Al6061. Error bars were found by calculating the standard deviation from four tests performed for each material type



## Discussion

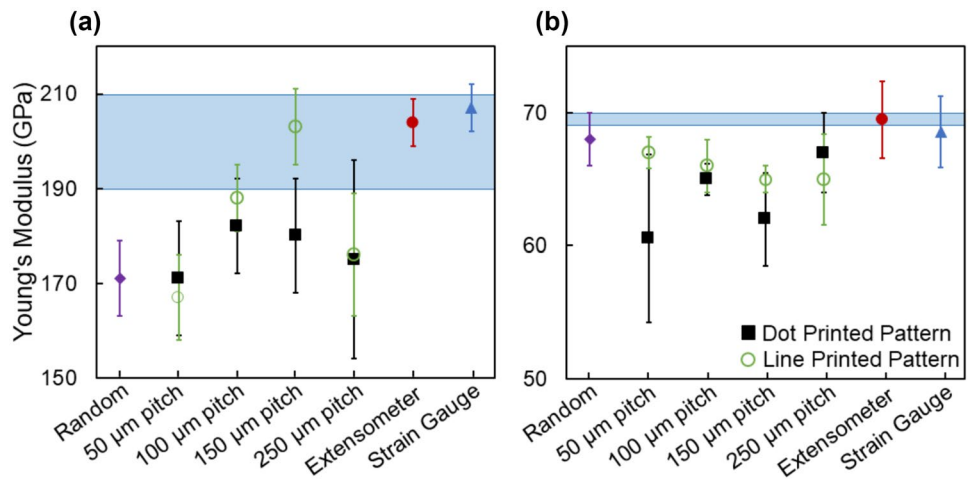
Based on the results observed from the patterns on SS316L (Fig. 5) and Al6061 (Fig. 6), images of periodic AJP fabricated patterns were successfully computed in a DIC algorithm and produced strain values that compared well to strain measurements recorded by the extensometer and strain gauges. More specifically, patterns with 100  $\mu\text{m}$  pitch dots and the 150  $\mu\text{m}$  pitch lines correlated to more accurate DIC strain measurements. The printed 100  $\mu\text{m}$  pitched dot and the 150  $\mu\text{m}$  pitched line patterns outperformed the other DIC patterns, likely due to their high grayscale contrast from added white speckles in the field of view (Fig. 4). A statistical analysis (Table 5) was used to then verify the strain values from the printed patterns aligned with the results from the extensometer.

All patterns processed using Ncorr lead to results that over-estimated the actual displacement experienced during testing. More specifically, the largest difference between the measured and actual displacement was observed at larger elongations (an exception to this was observed in the 100  $\mu\text{m}$  pitch and 50  $\mu\text{m}$  pitch lines on Al6061 substrates). A likely reason for the larger error at higher strains could be due to the type of strain being measurement between the Ncorr and the extensometer. Ncorr outputted results in Green-Lagrangian strains, while the extensometer measured in engineering strain, as discussed in “Image Analysis” section of this study. At small displacements ( $\leq 1000 \mu\epsilon$  or 0.001  $\epsilon$ ), the two corresponding strain types theoretically, measure elongation the same [70]; however, the relationship begins to deviate with increased displacements, as defined by the Seth-Hill family of strain tensors or also known

**Table 5** Relative maximum error and statistical significance values (*P*-value) of DIC patterns on SS316L and Al6061

Material Type	Printed Pattern Type	Pitch Sizes ( $\mu\text{m}$ )	Max. Error (%)	<i>P</i> -value
SS316L	Dots	50	32	0.37
		100	9	0.78
		150	27	0.44
		250	29	0.58
	Lines	50	27	0.42
		100	20	0.57
		150	11	0.61
		250	23	0.53
	<b>Spray-Painted Pattern</b>		20	0.48
Al6061	Dots	50	43	0.26
		100	2	0.99
		150	7	0.77
		250	13	0.73
	Lines	50	9	0.63
		100	5	0.95
		150	4	0.81
		250	8	0.81
	<b>Spray-Painted Pattern</b>		4	0.87

**Fig. 8** The Young’s modulus was found for all strain measurement methods on (a) SS316L and (b) Al6061 samples with Hooke’s Law (equation (2)). Error bars were derived from the standard deviation calculated from the tests performed with each pattern type and measurement method. The Young’s moduli were compared to values expected for SS316L and Al6061 [72–74]. Expected values (derived from literature values) are indicated by the highlighted regions in the plots



as the Doyle-Ericksen strain tensors. The Seth-Hill strain tensors are expressed as

$$\epsilon = \frac{1}{k}(x^k - 1) \tag{3}$$

where,  $\epsilon$  is the strain,  $k$  is a parameter defined by the type of strain tensor, and  $x$  is the final length ( $L$ ) divided by the original length ( $L_0$ ). For engineering strain ( $\epsilon_{eng}$ ), the parameter  $k$  is 1 and equation (3) simplifies to

$$\epsilon_{eng} = x - 1 = \frac{L - L_0}{L_0} \tag{4}$$

For Lagrangian strains ( $\epsilon_{Lag}$ ),  $k$  is equal to 2 and equation (3) becomes

$$\epsilon_{Lag} = \frac{1}{2}(x^2 - 1) \tag{5}$$

Elongation values should be in  $\epsilon$  and not  $\mu\epsilon$  when converting between equations (4) and (5). For high strain applications ( $>0.1\% \epsilon$ ), the Green-Lagrangian strain values would need to be converted to engineering strain to compare with the extensometer being used. In this study, samples were pulled to 1000–1100  $\mu\epsilon$ , which is at the threshold where differences in Green-Lagrangian strain and engineering strain is negligible. As such, the discrepancies between Green-Lagrangian and engineering strain

are minimal, but any tests performed at higher elongations should consider this error.

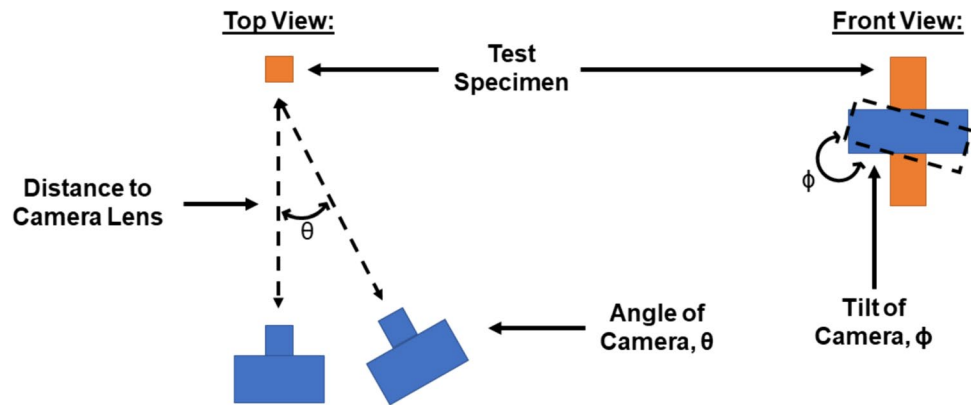
In addition, the uncertainty associated to strain results from the printed 100  $\mu\text{m}$  pitched dot and the 150  $\mu\text{m}$  pitched line patterns are within the actual strain experienced by the tensile specimens. For the other patterns, there were larger errors at higher strains, which means that differences between the DIC computed results and the strain measured by the extensometer is likely caused by pattern quality. From Fig. 4, patterns that had two distinct peaks in the black and white regions as well as minimal pixels in the gray-medium region of the grayscale intensity spectrum correlated to more accurate measurements.

Accordingly, there are inherent errors associated with 2D DIC experimental setups that have been previously studied [14, 26, 27, 75]. In order to optimize the experimental setup used in the following study, a variety of camera positions were explored, including changes in distance, angle ( $\theta$ ), and tilt ( $\phi$ ) from the perspective of the camera lens to the test specimen (Fig. 9). The results were computed from the 100  $\mu\text{m}$  pitch dot pattern and are shown in Fig. 10(a)–(d). Each change in position correlated to higher strain readings when compared to the extensometer and strain gauges. The optimal distance was determined to be approximately 60 mm with the camera lens that was used for testing (Fig. 10(e)). Other potential systematic errors with 2D DIC include distortion, pixilation, and random variation of brightness in

**Table 6** Coefficient of determination between DIC and extensometer

Printed Patterns	Dots				Lines				Spray-Painted Patterns	
	Pitch Sizes ( $\mu\text{m}$ )	250	150	100	50	250	150	100		50
SS316L, $R^2$		0.988	0.993	0.995	0.991	0.978	0.989	0.984	0.989	0.994
Al6061, $R^2$		0.993	0.993	0.995	0.978	0.992	0.992	0.985	0.989	0.985

**Fig. 9** Potential errors for 2D DIC during the experimental setup are caused by misalignment of the camera, such as out-of-plane displacement, angle, and tilt of the camera



images, which leaves strain fields to be highly susceptible for error [66]. In experimental mechanics, it is challenging to achieve the perfect setup, and as such, reducing error in strain measurements is an ongoing research area for those using 2D DIC [18, 26–28, 75].

Extensometers are classified from an A to an E, where class A extensometers have a fixed error that cannot exceed  $\pm 20 \mu\text{e}$  and class E extensometers have a fixed error of  $\pm 100,000 \mu\text{e}$  [64]. The type of extensometer desired depends on the testing environment and experimental requirements. While ASTM E2208-02 standard was created for evaluating non-contacting optical sensors in 2018 [65], there is no set method for calibrating DIC given the diverse measurement conditions and already established methods (e.g., strain gauges [76] and extensometers [64]) are necessary to assess the accuracy. As such, DIC strain readings in this study were directly compared to data recorded by strain gauges and an extensometer. Based on the results received, our DIC testing method would be considered a class B extensometer [64], which has a fixed error between 100 and 200  $\mu\text{e}$ .

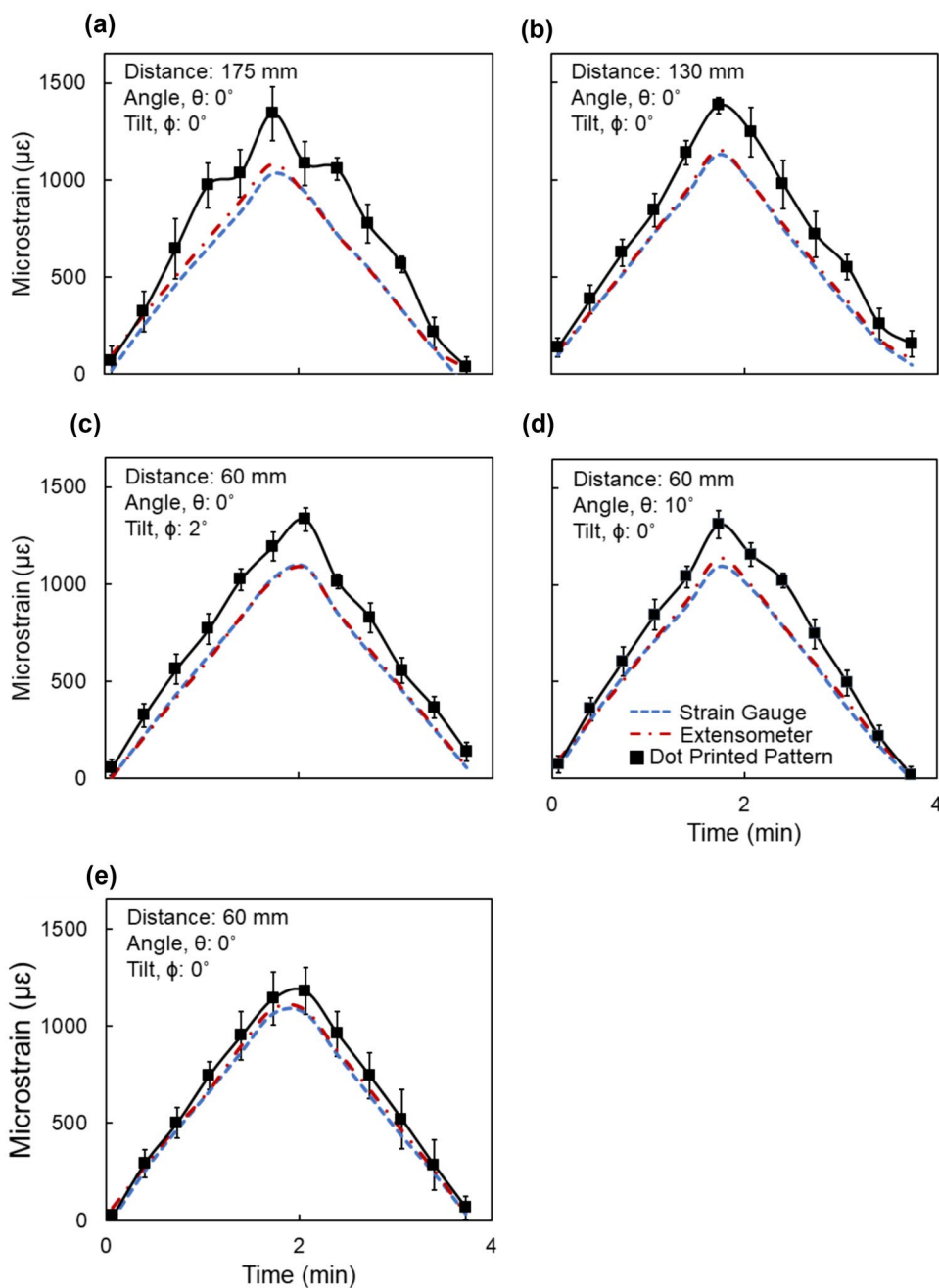
Using additive manufacturing capabilities in the pattern fabrication process brings DIC systems a step closer in terms of further standardization and commercialization. More specifically, AM achieves high contrast patterns with repeatability while also providing the user with an easier control over pattern quality compared to splattering techniques. AM also allows for the user to control the pattern design at different levels of randomness. Now, unlike other previous AM methods, such as inkjet printing used in Zhu et al. [43] and Koumlis et al. [44], aerosol jet printing has more customizable parameters, including changes in printing standoff distance and pressures, that allow for consistent patterns and adjustable for either 2D or 3D DIC applications. Zhu et al., reported having speckles sizes ranging from 90 to 150  $\mu\text{m}$  in diameter when using inkjet printing [43] and Yang et al. described their 3D printed random dot patterns to range from 100–200  $\mu\text{m}$  in speckle size [45]; however, AJP was able to print dots that were between 30 to 48  $\mu\text{m}$  in diameter across the four different pitch sizes used and were more circular in shape (Table 2). In addition, a variety of

ink-types can be used in aerosol jet printing unlike inkjet as discussed in the “Introduction” section. While there have been little to no studies that explore such direct print methods, AJP will be beneficial for DIC experimental setups with a need for a small form factor for various environments, such as aerospace and nuclear energy. AJP could use different ink-based materials to create a pattern that has corrosion resistance, irradiation resistance, and will withstand high temperature applications.

Lastly, this work tested the ability of Ncorr’s DIC algorithm to process images of repetitive patterns with low levels of randomness. Repetitive patterns using lines and dots are easily programmed into additive manufacturing software platforms, such as AJP; however, AM patterns may contain defects as observed in Fig. 2. Some of the dots are not an ideal circular shape and are considered defects. Defects are likely produced from an uneven background created by the black spray paint in this work. Defects may also occur from overspray in AJP systems [77], where some of the aerosolize nanoparticles escape from the ink-stream during printing and smaller particles are placed sporadically around the desired print shape. Such irregularities may contribute to the computational feasibility of periodic patterns fabricated using AJP. However, the patterns are still more periodic than they are random and this work demonstrates the ability of DIC to process patterns with low levels of randomness. In addition, DIC algorithms are continually advancing, which improves image analysis. DIC algorithms must make an initial guess to begin the iterative process for determining displacement and strain fields. Periodic patterns are inherently difficult for DIC because the program converges at local minimum when making the initial guess. Ncorr improves the initial guess by incorporating reliability-guided DIC technique into the IC-GN algorithm, as proposed by Pan et al. [78], where a center subset is placed in the middle of the region of interest. This subset is placed automatically in Ncorr, but can be moved if there exists a hole (or other degrading defect in the pattern) in the middle of the region of interest. The technique uses a scale-invariant feature transform [79] and normalized cross correlation [80] to find the initial guess



**Fig. 10** Experimental results when the camera was placed at four different positions: (a) 175 mm from sample, (b) 130 mm from sample, (c) titled ( $\phi$ ) 2° from sample, and (d) angled ( $\theta$ ) 10° from sample. The optimal position was when the camera was (e) 60 mm away from the test specimen. Error bars were found by finding the standard deviation at each measurement after three tests



by applying four surrounding seeds as explained in “Image Analysis” section. These methods make it possible to compute images of repetitive, lower random patterns by using more displacement parameters.

### Conclusion

Aerosol jet printing is a novel and effective method to fabricating repeatable micro-scale patterns for digital image correlation. More specifically, AJP offers a wide ink materials selection and suitable for a variety of substrate geometry that is desirable by

the nuclear energy field. This study explored the use of periodic patterns with different pitch spacing instead of the traditional random speckle pattern on two structural nuclear material systems (i.e., SS316L and Al6061). All DIC patterns were mechanically tested and verified using an extensometer and strain gauges. High contrast printed patterns had high accuracy when compared to the extensometer and strain gauges that were used to validate strain measurements during experiments. The printed 100  $\mu\text{m}$  pitch spacing and 150  $\mu\text{m}$  pitch spacing were correlated to strains with a maximum error between 2% and 11% for SS316L and Al6061. In addition, there was no significant difference between the strain values computed from any of the printed patterns and

the strain tracked by the extensometer. All patterns had a coefficient of determination above 0.97. To determine if the printed patterns were of good quality, mean intensity gradient and grayscale intensity analysis were performed. The results from this research concludes aerosol jet printing to be a viable technique for DIC pattern fabrication and Ncorr was able to resolve patterns with periodicity to provide high fidelity strain measurements. Accordingly, pattern fabrication with AJP for applications that require small fields of view will be beneficial when DIC is incorporated to harsh environment applications to monitor *in-situ* deformation. In addition, AJP will promote the reduction in innovation time for the aerospace and nuclear industries.

**Funding** This work was prepared as an account of work sponsored by the U.S. Department of Energy, Office of Nuclear Energy Advanced Sensors and Instrumentation program under DOE Contract DE-AC07-05ID14517. Additionally, this material was based upon work supported under a University Nuclear Leadership Program Graduate Fellowship through the U.S. Department of Energy, Office of Nuclear Energy.

## Declarations

**Conflict of Interest** The author(s) declared no known conflicts of interest with respect to the research, authorship, and/or publication of this article.

**Disclosure** Neither the U.S. Government nor any agency thereof, nor any of their employees, makes any warranty, expressed or implied, or assumes any legal liability or responsibility for the accuracy, completeness, or usefulness, of any information, apparatus, product, or process disclosed, or represents that its use would not infringe privately owned rights. References herein to any specific commercial product, process, or service by trade name, trademark, manufacturer, or otherwise, does not necessarily constitute or imply its endorsement, recommendation, or favoring by the U.S. Government or any agency thereof. The views and opinions of authors expressed herein do not necessarily state or reflect those of the U.S. Government or any agency thereof.

**Open Access** This article is licensed under a Creative Commons Attribution 4.0 International License, which permits use, sharing, adaptation, distribution and reproduction in any medium or format, as long as you give appropriate credit to the original author(s) and the source, provide a link to the Creative Commons licence, and indicate if changes were made. The images or other third party material in this article are included in the article's Creative Commons licence, unless indicated otherwise in a credit line to the material. If material is not included in the article's Creative Commons licence and your intended use is not permitted by statutory regulation or exceeds the permitted use, you will need to obtain permission directly from the copyright holder. To view a copy of this licence, visit <http://creativecommons.org/licenses/by/4.0/>.

## References

- Primer C et al (2020) Nuclear Energy Enabling Technologies (NEET): Advanced sensors and Instrumentation (ASI) program plan, INL/EXT-20-57280. United States, Idaho National Laboratory
- Skifton R et al (2017) In-pile fuel rod deformation measurements using miniaturized LVDT technology. Idaho National Laboratory (INL/EXT-17-43379-Rev000), Idaho Falls, Idaho
- Pettigrew MJ (2013) The behaviour of weldable strain gauges under nuclear reactor core conditions. Nucl Eng Des 263:350–361. <https://doi.org/10.1016/j.nucengdes.2013.06.008>
- Fujimoto KT et al (2020) Aerosol jet printed capacitive strain gauge for soft structural materials. npj Flex Electron 4(1):32. <https://doi.org/10.1038/s41528-020-00095-4>
- Phero TL et al (2022) Additively manufactured strain sensors for in-pile applications. Sens Actuators A Phys 344:113691. <https://doi.org/10.1016/j.sna.2022.113691>
- Extensometers (2022) MTS Systems, Minnesota, USA. <https://www.mts.com/-/media/materials/pdfs/brochures/mts-extensometer-catalog.pdf?as=1>
- Extensometer catalog, version 110.9.4 (2022) Epsilon Technology Corporation, Wyoming, USA. [https://www.epsilontech.com/wp-content/uploads/product-specs/Epsilon\\_extensometer\\_catalog.pdf](https://www.epsilontech.com/wp-content/uploads/product-specs/Epsilon_extensometer_catalog.pdf)
- Quanjin M et al (2020) Experimental investigation of the tensile test using digital image correlation (DIC) method. Mat Today Proc 27:757–763
- Pan B (2018) Digital image correlation for surface deformation measurement: historical developments, recent advances and future goals. Meas Sci Technol 29(8):082001. <https://doi.org/10.1088/1361-6501/aac55b>
- Park J et al (2017) Assessment of speckle-pattern quality in digital image correlation based on gray intensity and speckle morphology. Opt Lasers Eng 91:62–72. <https://doi.org/10.1016/j.optlaseng.2016.11.001>
- Peters WH, Ranson WF (1982) Digital imaging techniques in experimental stress analysis. Opt Eng 21(3):427–431. <https://doi.org/10.1117/12.7972925>
- Chu TC, Ranson WF, Sutton MA (1985) Applications of digital-image-correlation techniques to experimental mechanics. Exp Mech 25(3):232–244. <https://doi.org/10.1007/BF02325092>
- Sutton MA et al (1986) Application of an optimized digital correlation method to planar deformation analysis. Image Vis Comput 4(3):143–150. [https://doi.org/10.1016/0262-8856\(86\)90057-0](https://doi.org/10.1016/0262-8856(86)90057-0)
- Dong YL, Pan B (2017) A review of speckle pattern fabrication and assessment for digital image correlation. Exp Mech 57(8):1161–1181. <https://doi.org/10.1007/s11340-017-0283-1>
- Hassan GM (2021) Deformation measurement in the presence of discontinuities with digital image correlation: a review. Opt Lasers Eng 137:106394. <https://doi.org/10.1016/j.optlaseng.2020.106394>
- Pan B, Lu Z, Xie H (2010) Mean intensity gradient: an effective global parameter for quality assessment of the speckle patterns used in digital image correlation. Opt Lasers Eng 48(4):469–477. <https://doi.org/10.1016/j.optlaseng.2009.08.010>
- Blaysat B, Grédiac M, Sur F (2016) On the propagation of camera sensor noise to displacement maps obtained by DIC - an experimental study. Exp Mech 56(6):919–944. <https://doi.org/10.1007/s11340-016-0130-9>
- Haddadi H, Belhabib S (2008) Use of rigid-body motion for the investigation and estimation of the measurement errors related to digital image correlation technique. Opt Lasers Eng 46(2):185–196. <https://doi.org/10.1016/j.optlaseng.2007.05.008>
- Zheng Q, Mashiwa N, Furushima T (2020) Evaluation of large plastic deformation for metals by a non-contacting technique using digital image correlation with laser speckles. Mater Design 191:108626. <https://doi.org/10.1016/j.matdes.2020.108626>
- Lo C, Sano T, Hogan JD (2019) Microstructural and mechanical characterization of variability in porous advanced ceramics using X-ray computed tomography and digital image correlation. Mater Charact 158:109929. <https://doi.org/10.1016/j.matchar.2019.109929>
- Wang Y, Cuitiño AM (2002) Full-field measurements of heterogeneous deformation patterns on polymeric foams using digital image correlation. Int J Solids Struct 39(13):3777–3796. [https://doi.org/10.1016/S0020-7683\(02\)00176-2](https://doi.org/10.1016/S0020-7683(02)00176-2)
- Zhang D, Arola D (2004) Applications of digital image correlation to biological tissues. J Biomed Opt 9(4):691–699

23. Schreier HW, Garcia D, Sutton MA (2004) Advances in light microscope stereo vision. *Exp Mech* 44(3):278–288. <https://doi.org/10.1007/BF02427894>
24. Berfield TA et al (2007) Micro- and nanoscale deformation measurement of surface and internal planes via digital image correlation. *Exp Mech* 47(1):51–62. <https://doi.org/10.1007/s11340-006-0531-2>
25. Knauss WG, Chasiotis I, Huang Y (2003) Mechanical measurements at the micron and nanometer scales. *Mech Mater* 35(3):217–231. [https://doi.org/10.1016/S0167-6636\(02\)00271-5](https://doi.org/10.1016/S0167-6636(02)00271-5)
26. Pan B et al (2013) Systematic errors in two-dimensional digital image correlation due to lens distortion. *Opt Lasers Eng* 51(2):140–147. <https://doi.org/10.1016/j.optlaseng.2012.08.012>
27. Titkov VV, Panin SV (2019) Measurement affecting errors in digital image correlation. *IOP Conf Ser Mater Sci Eng* 511:012018. <https://doi.org/10.1088/1757-899x/511/1/012018>
28. Sutton MA et al (2008) The effect of out-of-plane motion on 2D and 3D digital image correlation measurements. *Opt Lasers Eng* 46(10):746–757. <https://doi.org/10.1016/j.optlaseng.2008.05.005>
29. Jones EMC, Iadicola MAE (2018) A good practice guide for digital image correlation. International Digital Image Correlation Society
30. Eichhorn GN et al (2020) Low-cost digital image correlation and strain measurement for geotechnical applications. *Strain* 56(6):e12348. <https://doi.org/10.1111/str.12348>
31. Mazzoleni P et al (2015) Thermo-mechanical toner transfer for high-quality digital image correlation speckle patterns. *Opt Lasers Eng* 75:72–80. <https://doi.org/10.1016/j.optlaseng.2015.06.009>
32. Quino G et al (2020) Speckle patterns for DIC in challenging scenarios: rapid application and impact endurance. *Meas Sci Technol* 32(1):015203. <https://doi.org/10.1088/1361-6501/abaee8>
33. Lionello G, Cristofolini L (2014) A practical approach to optimizing the preparation of speckle patterns for digital-image correlation. *Meas Sci Technol* 25(10):107001. <https://doi.org/10.1088/0957-0233/25/10/107001>
34. Wang H et al (2012) Fabrication of micro-scale speckle pattern and its applications for deformation measurement. *Meas Sci Technol* 23(3):035402. <https://doi.org/10.1088/0957-0233/23/3/035402>
35. Jonnalagadda KN et al (2010) Experimental investigation of strain rate dependence of nanocrystalline pt films. *Exp Mech* 50(1):25–35. <https://doi.org/10.1007/s11340-008-9212-7>
36. Scrivens WA et al (2007) Development of patterns for digital image correlation measurements at reduced length scales. *Exp Mech* 47(1):63–77. <https://doi.org/10.1007/s11340-006-5869-y>
37. Li N, Guo S, Sutton M (2011) Recent progress in e-beam lithography for SEM patterning. pp 163–166
38. Sabaté N et al (2006) Digital image correlation of nanoscale deformation fields for local stress measurement in thin films. *Nanotechnology* 17(20):5264–5270. <https://doi.org/10.1088/0957-4484/17/20/037>
39. Grant BMB et al (2009) High-temperature strain field measurement using digital image correlation. *J Strain Anal Eng Des* 44(4):263–271. <https://doi.org/10.1243/03093247jsa478>
40. Meyer P, Waas AM (2015) Measurement of *in situ*-full-field strain maps on ceramic matrix composites at elevated temperature using digital image correlation. *Exp Mech* 55(5):795–802. <https://doi.org/10.1007/s11340-014-9979-7>
41. Hu YJ et al (2018) A new method of creating high-temperature speckle patterns and its application in the determination of the high-temperature mechanical properties of metals. *Exp Tech* 42(5):523–532. <https://doi.org/10.1007/s40799-018-0256-z>
42. Seifert T et al (2015) Additive manufacturing technologies compared: morphology of deposits of silver ink using inkjet and aerosol jet printing. *Ind Eng Chem Res* 54(2):769–779. <https://doi.org/10.1021/ie503636c>
43. Zhu K, Li C, Pan B (2022) Rapid and repeatable fluorescent speckle pattern fabrication using a handheld inkjet printer. *Exp Mech* 62(4):627–637. <https://doi.org/10.1007/s11340-021-00814-6>
44. Koumlis S et al (2019) Drop on demand colloidal suspension inkjet patterning for DIC. *Exp Tech* 43(2):137–148
45. Yang J, Tao JL, Franck C (2021) Smart digital image correlation patterns via 3D printing. *Exp Mech* 61(7):1181–1191. <https://doi.org/10.1007/s11340-021-00720-x>
46. Wilkinson NJ et al (2019) A review of aerosol jet printing—a non-traditional hybrid process for micro-manufacturing. *Int J Adv Manuf Technol* 105(11):4599–4619. <https://doi.org/10.1007/s00170-019-03438-2>
47. Grédiac M, Blaysat B, Sur F (2020) On the optimal pattern for displacement field measurement: random speckle and DIC, or checkerboard and LSA? *Exp Mech* 60(4):509–534. <https://doi.org/10.1007/s11340-019-00579-z>
48. Shi Y et al (2022) Designing patterns for DIC with poisson image editing. *Exp Mech* 62(7):1093–1117. <https://doi.org/10.1007/s11340-022-00862-6>
49. Parks VJ (1969) The grid method. *Exp Mech* 9(7):27N–33N. <https://doi.org/10.1007/BF02325141>
50. Wang Z et al (2019) DIC/Moire hybrid method based on regular patterns for deformation measurement. *Opt Express* 27(13):18435–18444. <https://doi.org/10.1364/OE.27.018435>
51. Grédiac M, Sur F, Blaysat B (2016) The grid method for in-plane displacement and strain measurement: a review and analysis. *Strain* 52(3):205–243. <https://doi.org/10.1111/str.12182>
52. Grédiac M, Blaysat B, Sur F (2017) A critical comparison of some metrological parameters characterizing local digital image correlation and grid method. *Exp Mech* 57(6):871–903. <https://doi.org/10.1007/s11340-017-0279-x>
53. Saletti D, Forquin P (2016) A comparison of DIC and grid measurements for processing spalling tests with the VFM and an 80-kpixel ultra-high speed camera. *Eur Phys J Spec Top* 225:311–323
54. ASTM (2020) E8/E8M – 16a: Standard test methods for tension testing of metallic materials. pp 1–30
55. Gussev MN et al (2021) Influence of neutron irradiation on Al-6061 alloy produced via ultrasonic additive manufacturing. *J Nucl Mater* 550:152939. <https://doi.org/10.1016/j.jnucmat.2021.152939>
56. Was GS et al (2007) Corrosion and stress corrosion cracking in supercritical water. *J Nucl Mater* 371(1):176–201. <https://doi.org/10.1016/j.jnucmat.2007.05.017>
57. Nezakat M et al (2015) Effect of thermo-mechanical processing on oxidation of austenitic stainless steel 316L in supercritical water. *Corros Sci* 94:197–206. <https://doi.org/10.1016/j.corsci.2015.02.008>
58. Smith M et al (2017) Controlling and assessing the quality of aerosol jet printed features for large area and flexible electronics. *Flex Print Electron* 2(1):015004. <https://doi.org/10.1088/2058-8585/aa5af9>
59. Jing Q et al (2019) Freestanding functional structures by aerosol-jet printing for stretchable electronics and sensing applications. *Adv Mater Technol* 4(7):1900048. <https://doi.org/10.1002/admt.201900048>
60. Saleh MS et al (2021) 3D printed three-dimensional metallic microlattices with controlled and tunable mechanical properties. *Addit Manuf* 39:101856. <https://doi.org/10.1016/j.addma.2021.101856>
61. Wadhwa A, Cormier D, Williams S (2016) Improving run-time stability with aerosol jet printing using a solvent add-back bubbler. *J Print Media Technol Res* 5:769–779
62. Schneider CA, Rasband WS, Eliceiri KW (2012) NIH image to ImageJ: 25 years of image analysis. *Nat Methods* 9(7):671–675. <https://doi.org/10.1038/nmeth.2089>
63. ASTM (2014) E251–92: Standard test methods for performance characteristics of metallic bonded resistance strain gauges. pp 433–452
64. ASTM (2017) E83–16: Standard practice for verification and classification of extensometer systems. pp 264–277
65. ASTM (2018) E2208–02: Standard guide for evaluating non-contacting optical strain measurement systems. pp 1–7

66. Blaber J, Antoniou A (2017) Ncorr: instruction manual. Georgia Institute of Technology
67. Pan B, Li K, Tong W (2013) Fast, robust and accurate digital image correlation calculation without redundant computations. *Exp Mech* 53(7):1277–1289. <https://doi.org/10.1007/s11340-013-9717-6>
68. Liu M et al (2019) Application of digital image correlation (DIC) to the measurement of strain concentration of a PVA dual-crosslink hydrogel under large deformation. *Exp Mech* 59(7):1021–1032. <https://doi.org/10.1007/s11340-019-00520-4>
69. Xing JQ, Zhao C, Zhou YM (2020) Strain localization in hydraulic fracturing of granite specimens based on DIC method. *IOP Conf Ser Earth Environ Sci* 570(3):032031. <https://doi.org/10.1088/1755-1315/570/3/032031>
70. Okereke M, Keates S (2018) Material response: measures of stress and strain. In: *Finite element applications: a practical guide to the FEM process*. Springer International Publishing, Cham, pp 299–362
71. Barranger Y et al (2010) Digital image correlation accuracy: influence of kind of speckle and recording setup. *EPJ Web Conf* 6:31002
72. Boyer H, Gall T (1985) *Metals handbook*. American Society for Metals, Novelty, OH
73. Lackey A (2016) Comparative study of mechanical properties of 316L stainless steel between traditional production methods and selective laser melting. In: *Department of Engineering and Technology*. Western Carolina University
74. Röttger A et al (2020) Microstructure and mechanical properties of 316L austenitic stainless steel processed by different SLM devices. *Int J Adv Manuf Technol* 108(3):769–783. <https://doi.org/10.1007/s00170-020-05371-1>
75. Zhao J, Sang Y, Duan F (2019) The state of the art of two-dimensional digital image correlation computational method. *Eng Rep* 1(2):e12038. <https://doi.org/10.1002/eng2.12038>
76. ASTM (2014) E251–92: Standard test methods for performance characteristics of metallic bonded resistance strain gauges. pp 433–452
77. Chen G et al (2018) The effect of droplet sizes on overspray in aerosol-jet printing. *Adv Eng Mater* 20(8):1701084. <https://doi.org/10.1002/adem.201701084>
78. Pan B, Dafang W, Yong X (2012) Incremental calculation for large deformation measurement using reliability-guided digital image correlation. *Opt Lasers Eng* 50(4):586–592. <https://doi.org/10.1016/j.optlaseng.2011.05.005>
79. Wang Z et al (2014) Automated fast initial guess in digital image correlation. *Strain* 50(1):28–36. <https://doi.org/10.1111/str.12063>
80. Lewis JP (1995) Fast normalized cross-correlation. In: *Proceedings of vision interface*. pp 120–123

**Publisher's Note** Springer Nature remains neutral with regard to jurisdictional claims in published maps and institutional affiliations.